

F. THE PHOBOS EXPERIMENT AT RHIC

(B. B. Back, A. H. Wuosmaa, and the PHOBOS Collaboration*)

The PHOBOS experiment has made significant progress over the past year. Much of the effort was devoted to the analysis and interpretation of data obtained during RHIC runs 1 and 2, while also obtaining new results from the run 3 d + Au data at $\sqrt{s_{NN}} = 200$ GeV. The study of this asymmetric system provided an important control for Au + Au collisions, which showed strong suppression of high- p_T particles. No such suppression was observed for the d + Au data indicating that the suppression in Au + Au collisions was indeed an exit channel effect associated with the opacity of the matter formed only in these collisions. This result, which was obtained simultaneously by all four RHIC experiments, was viewed as a major milestone on the road to discovery of the quark-gluon plasma. Consequently, it was announced at a day-long press conference and symposium on June 18, 2003 sponsored by the Department of Energy and Brookhaven National Laboratory. Papers from the four experiments were published in the August 2003 issue of Physical Review Letters.

f.1. Charged Particle Multiplicity in Au + Au Collisions

Multiplicity Distributions

The pseudorapidity distributions, $dN_{ch}/d\eta$ are shown as solid points in Figs. I-38 and I-39 for different centrality bins, where the shaded bands represent the range of systematic errors to the 90% confidence-level. All $dN_{ch}/d\eta$ distributions exhibit a plateau around $\eta \sim 0$, the range of which increases with increasing collision energy from $\sqrt{s_{NN}} = 19.6$ to $\sqrt{s_{NN}} = 200$ followed by a smooth fall-off to higher values of η . Also the fall-off, which is associated with the fragmentation region, is increasing in range with energy. It is also apparent that the level of the central plateau increases with both centrality and collision energy. The open points represent the mid-rapidity values $dN_{ch}/d\eta|_{|\eta|<1}$ obtained from the tracklet counting method. Solid curves in Fig. I-38 represent a double Gaussian fit to the data in the range $-3 < \eta < 3$, whereas the solid curves in Fig. I-39 were obtained by a triple Gaussian fit to the data over the whole measured range of η . Note that for $\sqrt{s_{NN}} = 19.6$ GeV the data exceed the fitted curves in the large $|\eta|$ region,

especially for peripheral collisions. This deviation is discussed below.

The charged particle multiplicity at mid-rapidity, $dN_{ch}/d\eta|_{|\eta|<1}$, normalized to the number of participant nucleon pairs, $\langle N_{part}/2 \rangle$, are compared to lower energy measurements of Au + Au and Pb + Pb collisions in Fig. I-40a for the 6% most central collisions. We observe that the heavy-ion data appear to follow an energy dependence that is linear in $\ln(s^{1/2})$ as indicated by the solid line, *i.e.*

$$dN_{ch}/d\eta / \langle N_{part}/2 \rangle = -0.383 + 0.771 \ln(s^{1/2}).$$

Above $s^{1/2} \sim 20$ GeV, however, the data are also consistent with the predictions of the Gluon Saturation Model as indicated by the dashed curve.

Nearly all produced charged particles fall within the acceptance of PHOBOS. Therefore it is appropriate to integrate the $dN_{ch}/d\eta$ distributions in order to estimate the total number of charged particles emitted within this range. These estimates, obtained by an extrapolation into the unmeasured region, are shown as solid squares in Fig. I-40b.

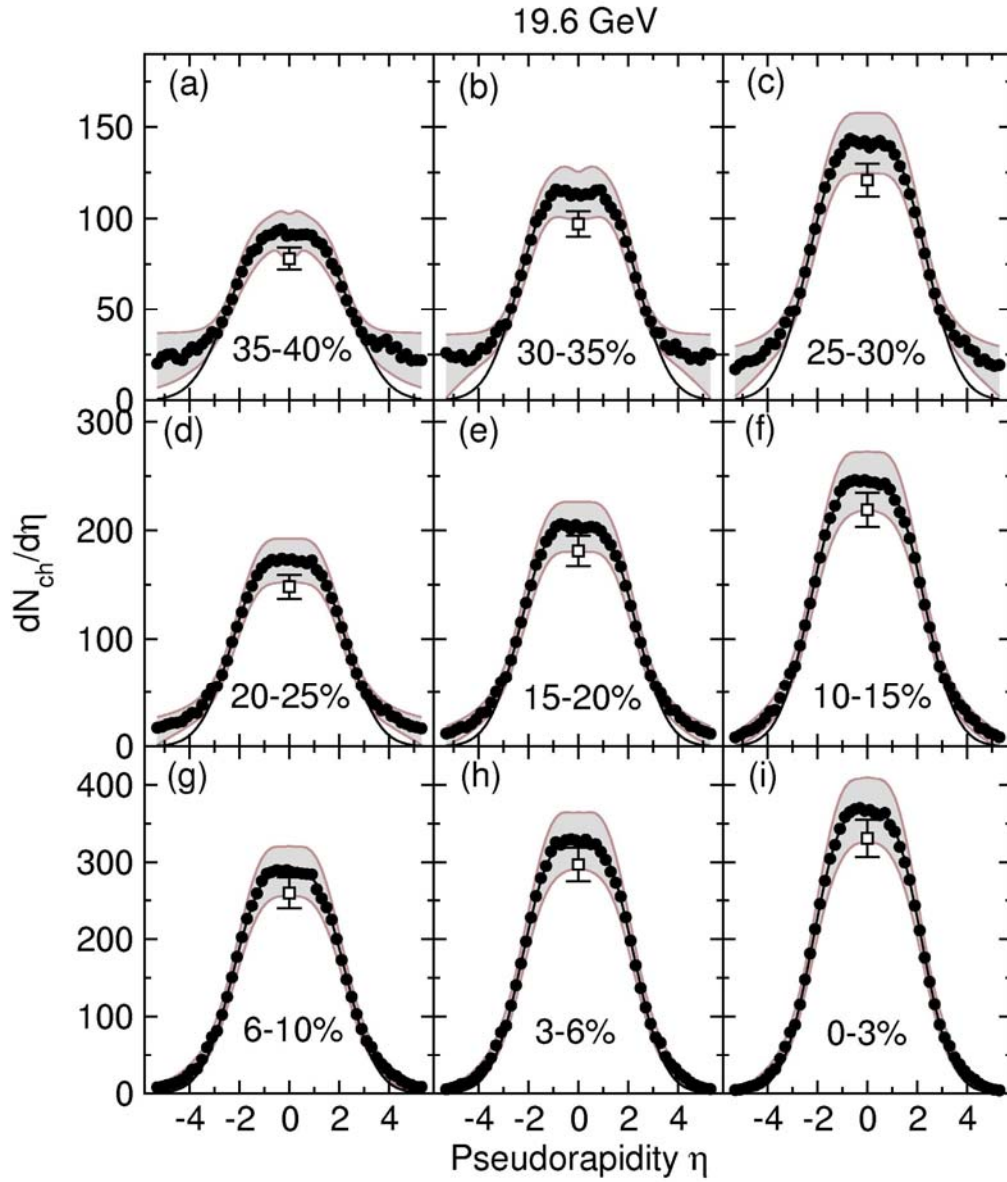


Fig. I-38. $dN_{ch}/d\eta$ vs η (solid points) for nine centrality bins representing 40% of the total cross section for $\sqrt{s_{NN}} = 19.6$ GeV. The solid curve is a symmetric double-Gaussian function fit to the data within the $-3 < \eta < 3$ region. The shaded band represent estimated systematic errors. The open points were obtained by the tracklet analysis for events in the range $|\eta| < 1$.

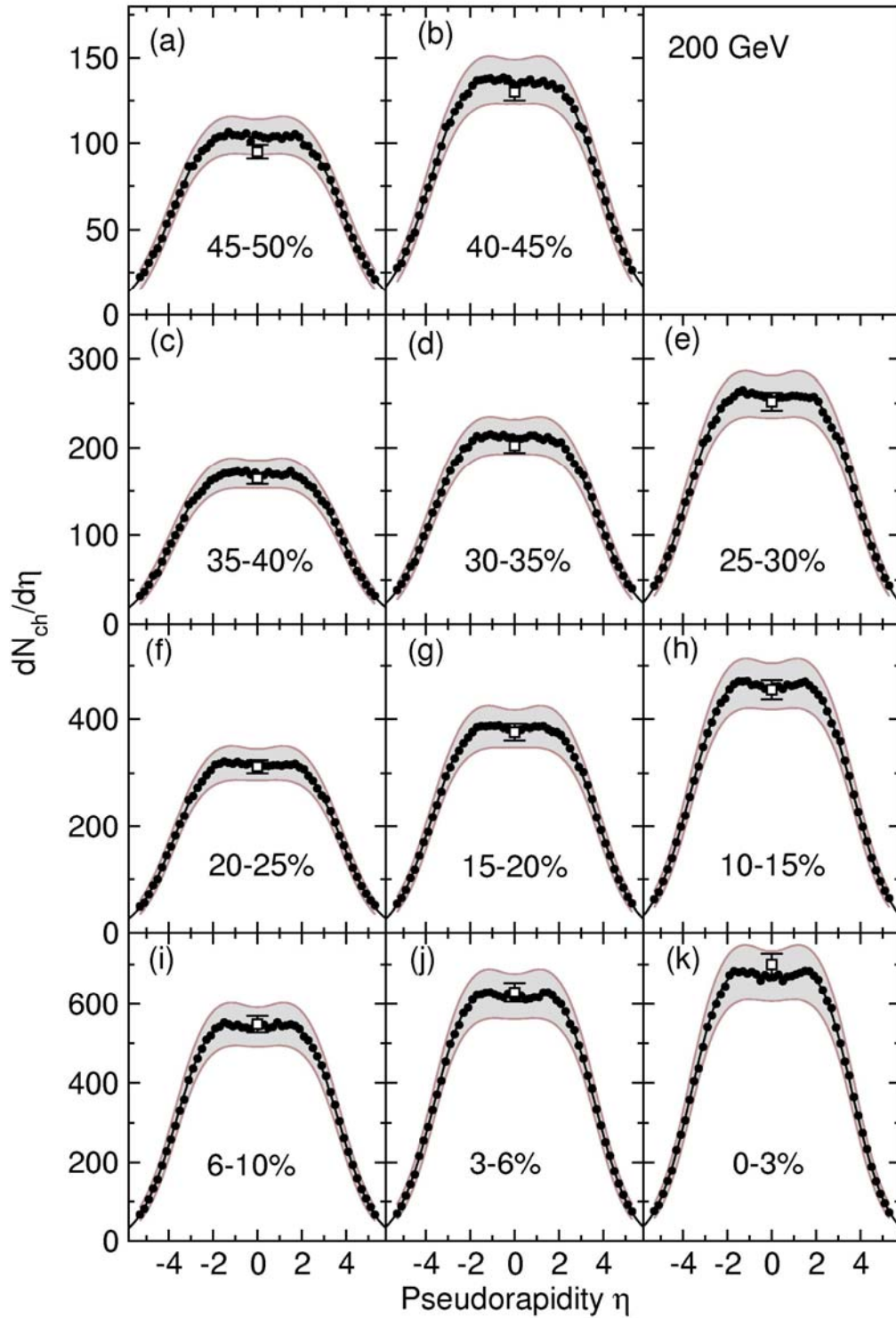


Fig. I-39. Same as Fig. I-38 but for $\sqrt{s_{NN}} = 200$ GeV and with a triple Gaussian fit (solid curve) to the data over the full acceptance region $|\eta| < 5.4$.

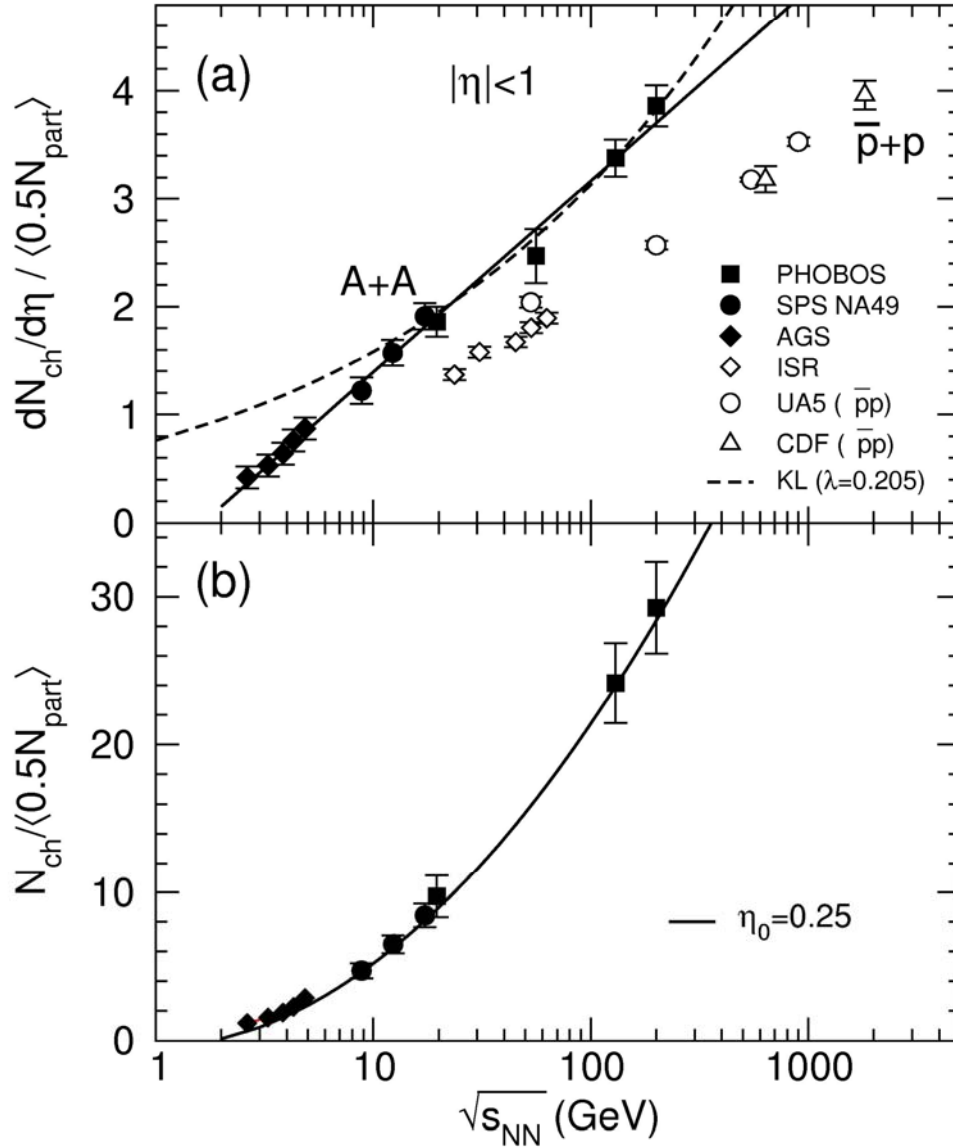


Fig. I-40. Panel a): The energy dependence of the charged particle $dN_{ch}/d\eta / \langle N_{part}/2 \rangle$ at mid-rapidity $|\eta| < 1$ for 0-6% central collisions is shown for nucleus-nucleus (solid symbols) and p + p (open diamond)⁶ and p + p-bar collisions (open circles² open triangles).⁷ The solid squares represent results from the PHOBOS experiment; 56 GeV⁸ and the present work, respectively. The solid line is a linear fit to the data (see text), whereas the dashed curve represents a saturation model calculations using with parameters listed in the text. Panel b): The total charged particle multiplicity per participant pair, $\langle N_{part}/2 \rangle$, is shown as a function of collision energy $\sqrt{s_{NN}}$ for central (0 - 6%) Au + Au collisions (solid squares, present work and solid circles).⁹ The solid curve represents a fit to the data using Eq. 12 with parameters given in the text.

Limiting Fragmentation

Limiting fragmentation scaling was recently observed¹ in Au + Au collisions, which corroborates a similar feature seen in nucleon-nucleon collisions over a wide energy region.² This feature is illustrated in Fig. I-41 where the charged particle multiplicity is plotted against an offset pseudorapidity parameter $\eta' = \eta \pm y_{\text{beam}}$, where y_{beam} is the rapidity of the Au-beam proceeding in the positive z direction. It is evident that the distributions, shifted in this manner, coincide very well in the overlap region around $\eta' \sim 0$. One observes that the mid-rapidity plateau increases in both height and width as the beam rapidity is increased. Also the η -range of the limited fragmentation region increases considerably with energy. In fact, the $dN_{\text{ch}}/d\eta$ appears to follow a universal curve from the $\eta' = 0$ point toward midrapidity breaking away from this curve at higher values of $dN_{\text{ch}}/d\eta$ with increasing collision energy. The solid lines in Fig. I-41 illustrate the fact that $dN_{\text{ch}}/d\eta$ in central collisions increases almost linearly at a rate of $\alpha = 195$ charged particles per unit pseudorapidity in this region, independent of collision energy.

Based on the regular features of both the height of the central plateau as well as the predictable nature of the fragmentation region we have developed a simple semi-empirical expression for the total charged particle multiplicity in central Au + Au collisions. Assuming an approximate trapezoidal shape of the $dN_{\text{ch}}/d\eta$ distributions, one may thus expect an expression of the form

$$N_{\text{ch}} = dN_{\text{ch}}/d\eta (\eta_0 + 2y_{\text{beam}} - dN_{\text{ch}}/d\eta/\alpha),$$

where $\eta_0 = 0.25$ is an offset width, the term $y_{\text{beam}} = \text{atanh}[(1 - 4m_0^2/s)^{1/2}]$ accounts for the increased width of the distribution as a function of collision energy, m_0 is the nucleon mass and $\alpha = 195$ is the slope of the pseudorapidity distribution in the fragmentation region. This expression, shown as the solid curve in Fig. I-40b, is seen to provide a good description of the total charged particle production over the entire energy region from 2.5 to 200 GeV.

Spectator Emission at $\sqrt{s_{NN}} = 19.6 \text{ GeV}$

In this section it is argued that the wings observed in the peripheral collisions at $\sqrt{s_{NN}} = 19.6 \text{ GeV}$ arise from particles emitted from the collision spectators. In an attempt to isolate the spectator contribution to the $dN_{\text{ch}}/d\eta$ distribution we subtract the fit in the $-3 < \eta < 3$ range from the measured $dN_{\text{ch}}/d\eta$ distribution resulting in the solid points in Fig. I-42. The shaded bands represent the systematic error of the data. The error

associated with the double Gaussian fit to the data in the $-3 < \eta < 3$ range is negligible.

We now explore the consequences of a simple model in which thermal equilibrium is established in the spectator, which proceeds to emit all of its protons isotropically in its rest frame according to a Boltzmann distribution. The expected $dN_{\text{ch}}/d\eta$ distributions for thermal emission from a spectator traveling along the beam-line with rapidity $y_0 = 3.04$ corresponding to $\sqrt{s_{NN}} = 19.6 \text{ GeV}$ for spectator temperatures of 5 and 15 MeV are found to fall partly within the detector acceptance $|\eta| < 5.4$, whereas emission from spectators moving with $y_0 = 5.36$ ($\sqrt{s_{NN}} = 200 \text{ GeV}$) falls outside the measured region. It therefore appears plausible that the wings of the $dN_{\text{ch}}/d\eta$ distribution seen only at $\sqrt{s_{NN}} = 19.6 \text{ GeV}$ originate from spectator emission provided that temperatures in the 5 - 15 MeV range may be expected.

We estimated the spectator temperature in two models. The Goldhaber projectile fragmentation model³ provides an estimate of momentum dispersion and the temperature of the spectator by considering the momentum distribution of the constituent nucleons prior to the break-up. This model leads to a nuclear temperature of $T = 15 \text{ MeV}$, which is independent of the size of the spectator, and consequently N_{part} . Assuming that all spectator protons, *i.e.* $N_{\text{spec}} = (394 - N_{\text{part}}) \times 79/197$, are emitted at a temperature of $T = 15 \text{ MeV}$, half of them from each spectator, we obtain the solid curves in Fig. I-42. Although the predicted spectator contributions are seen to be somewhat narrower than the data, they fall in the correct region of η . Also the total number of charged particles emitted from the spectators is roughly correct.

Secondly, one may estimate the excitation energy of the spectator from the Liquid Drop Model⁴ by accounting for the change in nuclear binding between the spectator shape (a cylindrical cut off a sphere) and the spherical ground state of the relaxed spectator nucleus. Predictably, this model leads to a lower estimate of the excitation energy between 3.6 to 11 MeV for $N_{\text{part}} = 103$ to 351, respectively, since this model does not take into account the disruption to the momentum distribution of the spectator nucleus caused by the collision, but only accounts for the subsequent heating arising from the shape change.

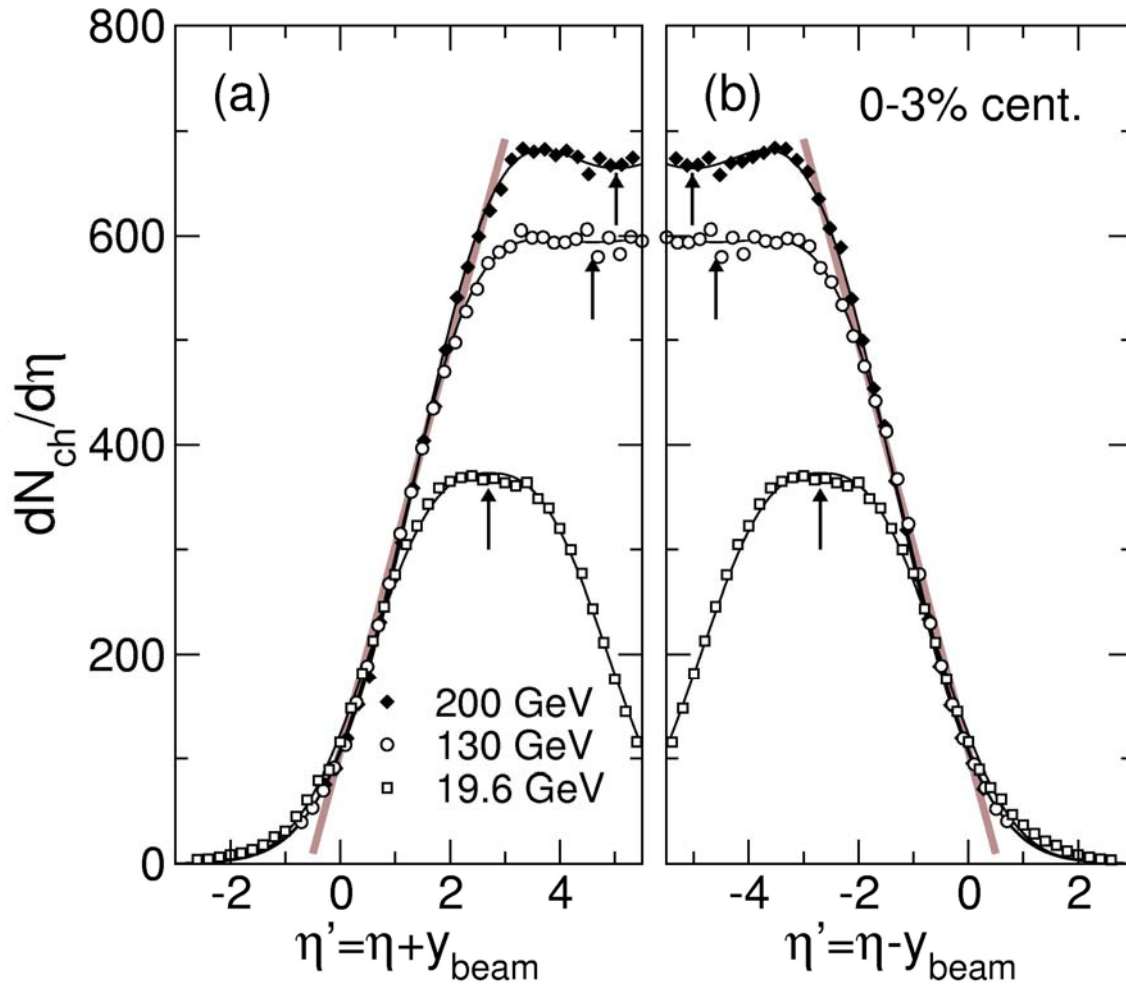


Fig. I-41. Illustration of the limiting fragmentation scaling in Au + Au collisions. $dN_{ch}/d\eta$ is shown as a function of the parameter $\eta' = \eta - y_{beam}$. Panels a) and b) show the limiting fragmentation scaling in the negative and positive pseudorapidity directions, respectively.

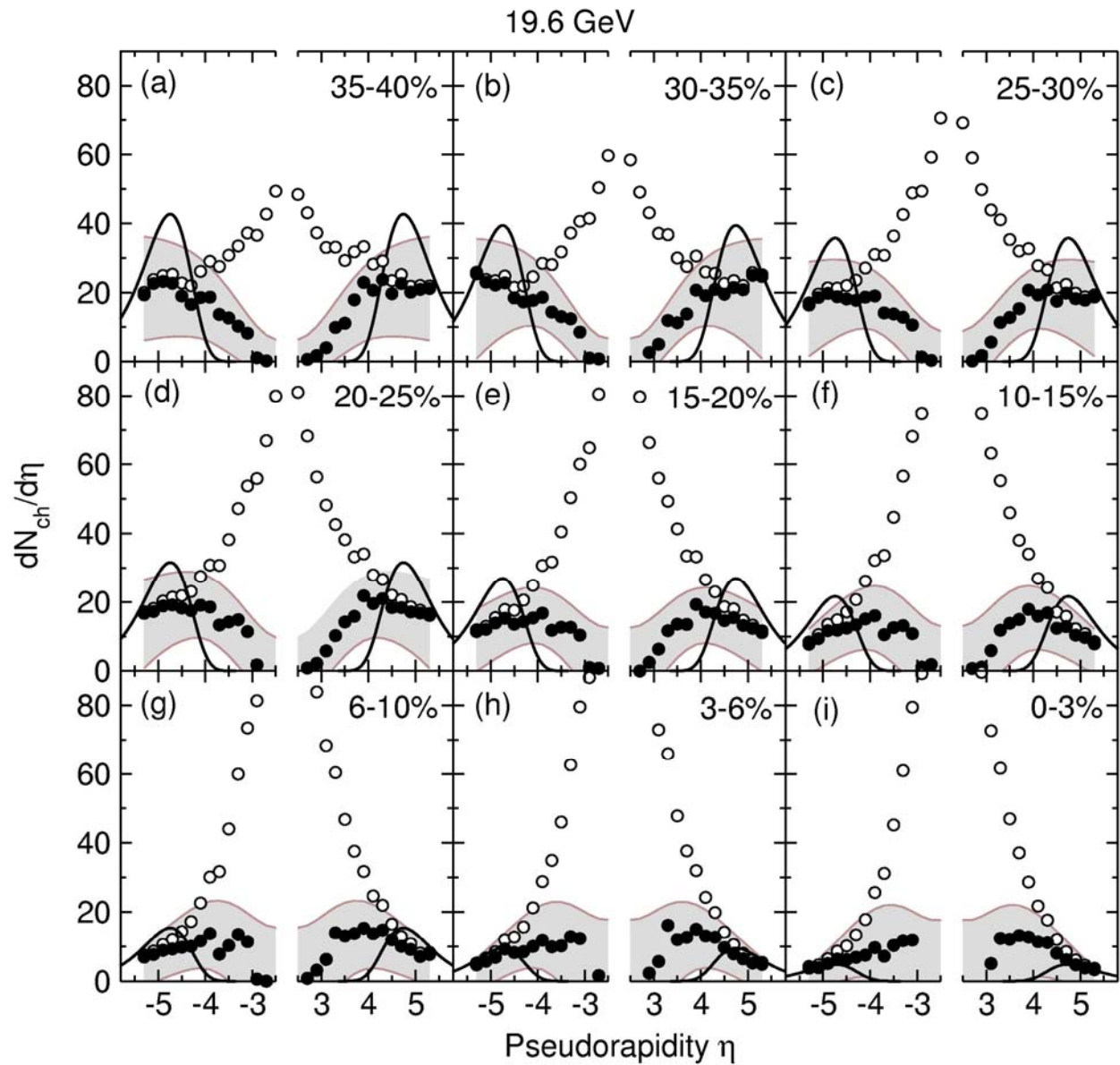


Fig. I-42. Comparison of estimated spectator contribution (solid points) with the simple model prediction (solid curves) as described in the text. The open points represent the measured $dN_{ch}/d\eta$ distribution. Note the break in the abscissa scale.

Despite the simplicity of this model as well as the large uncertainty on the estimated spectator component, it is felt that spectator emission is the most plausible explanation for the observed wings in the $dN_{ch}/d\eta$ distributions at $\sqrt{s_{NN}} = 19.6$ GeV. Such a contribution should be expected and it was indeed observed in earlier fixed target experiments at AGS energies, where Barrette *et al.*⁵ have measured the p_T distribution of neutrons emitted at beam rapidity for 14.5 GeV/nucleon Si + Pb and found that the spectrum is well represented by the Goldhaber model. It should

be noted that spectator emission is not expected to contribute significantly to the fragmentation region for the central collisions.

The charged particle multiplicities in relativistic Au + Au collisions obtained by the PHOBOS collaboration will be the subject of a Physical Review paper, which is nearing completion. This article is intended to include all relevant aspects of these measurements which include data obtained at 19.6, 130, and 200 GeV.

f.2. Charged Particle Multiplicity in D + Au Collisions

Charged particle multiplicity data on d + Au collisions at $\sqrt{s_{NN}} = 200$ GeV were obtained from the RHIC run 3, which took place in the winter of 2003. The first analysis was completed to obtain the minimum bias distribution of charged particles as a function of pseudorapidity. Special care was taken to obtain a reliable measure of the number of participants, N_{part} , in the collision and correct for the detection and reconstruction efficiency, which depends strongly on N_{part} . In Fig. I-43 we compare the $dN/d\eta$ obtained in the d + Au reaction (solid circles) to those from p + p (open squares) and Au + Au (open triangles) collisions. The distributions were normalized to the number of participating nucleon pairs $N_{part}/2$. It is clear that the asymmetric nature of the d + Au reactions affects the particle emission pattern in the d + Au reaction, which is substantially stronger in the direction of the incoming Au nucleus. Glauber model calculations show that the number of nucleons in the Au nucleus, N_{part}^{Au} , on average is 3 - 4 times larger than the number of participating deuteron nucleons, N_{part}^d . It therefore appears that this asymmetry to a significant degree can be ascribed to simple momentum conservation.

The total number of charged particles, N_{ch} , emitted in minimum bias d + Au collisions was estimated by extrapolation into the unmeasured region of η . Using an extrapolation guided by theoretically predicted

shapes we find $N_{ch} = 87_{-7}^{+23}$. It is however expected that a more precise upper limit can be achieved by a detailed analysis of the centrality dependence of the particle production.

The measured $dN/d\eta$ distribution is compared with various theoretical predictions in Fig. I-44. We observe that the Parton Saturation Model¹¹ (solid curve, panel a) substantially overpredicts the forward-backward asymmetry of the particle emission, whereas the Relativistic Quantum-Molecular Dynamics (RQMD) model¹⁰ underpredicts the total particle production. The HIJING¹² model (dashed-dotted curve, panel b) appears to approximate the measured shape, especially when the final state interactions are included in the AMPT¹³ variant of this model (dashed and solid curves, panel b).

f.3. Transverse Momentum Spectra: Comparison of D + Au to Au + Au

A central result of the 200 GeV Au + Au measurements of RHIC Run 2, was the observation (by all four experiments) of a substantial suppression of the high- p_T part of both neutral and charged particle spectra in central collisions. One plausible explanation of this deficit of high energy particles, when normalized to pp

data, derives from the assumption of a strong energy loss mechanism of partons traversing a colored high density medium formed in the heavy ion collisions. This observation may therefore be taken as an early tentative indication of a transition to a quark-gluon plasma phase in central Au + Au collisions.

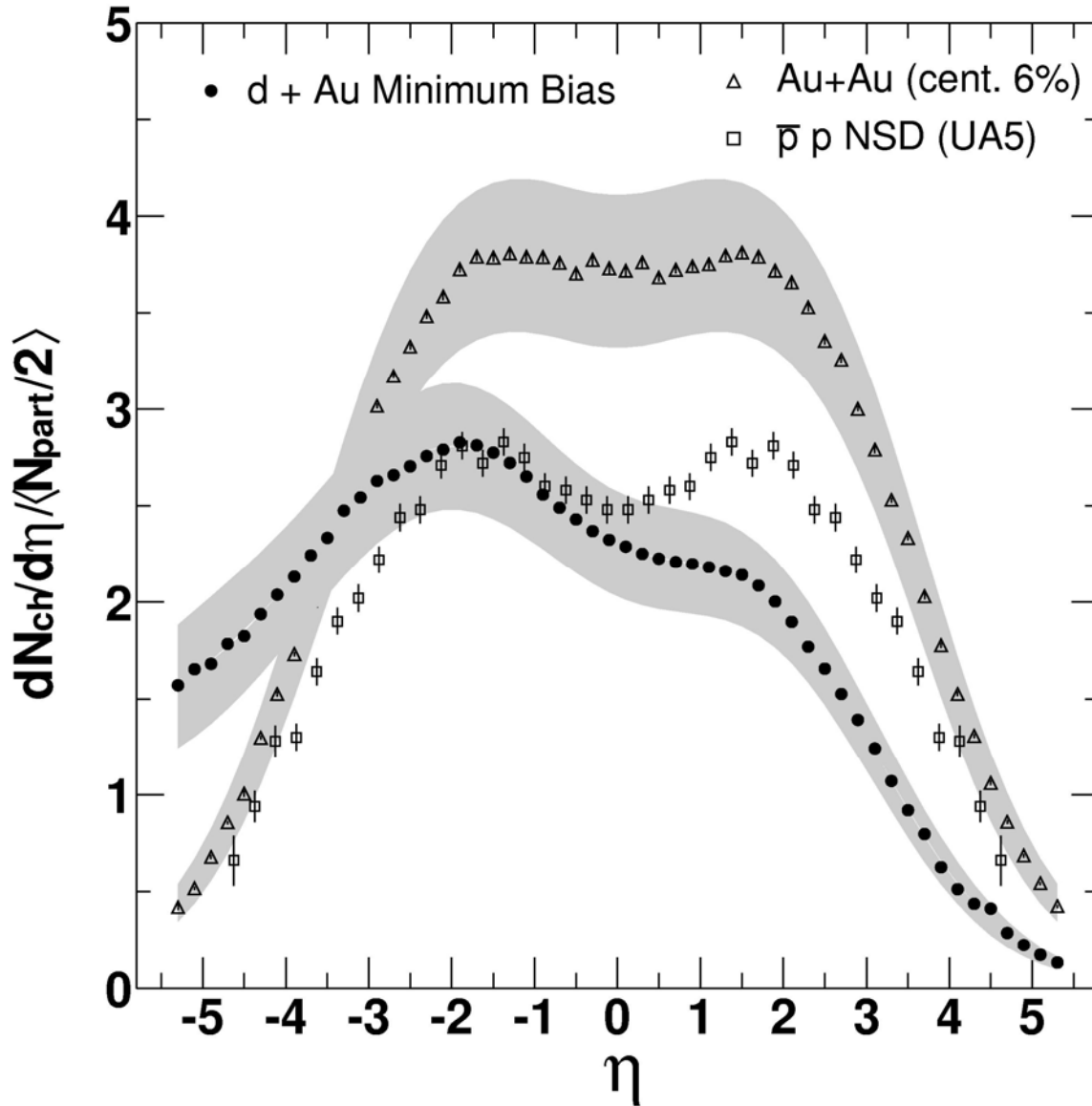


Fig. I-43. $dN_{ch}/d\eta$ distribution per participant pair for minimum-bias dAu collisions at $\sqrt{s_{NN}} = 200$ GeV, for central $AuAu$ collisions (0 - 6%) and for pp collisions from UA5² at the same energy. The systematic errors are shown by the gray bands. The dAu and $AuAu$ distributions have 8% scale uncertainty from the error on the $\langle N_{part}/2 \rangle$.

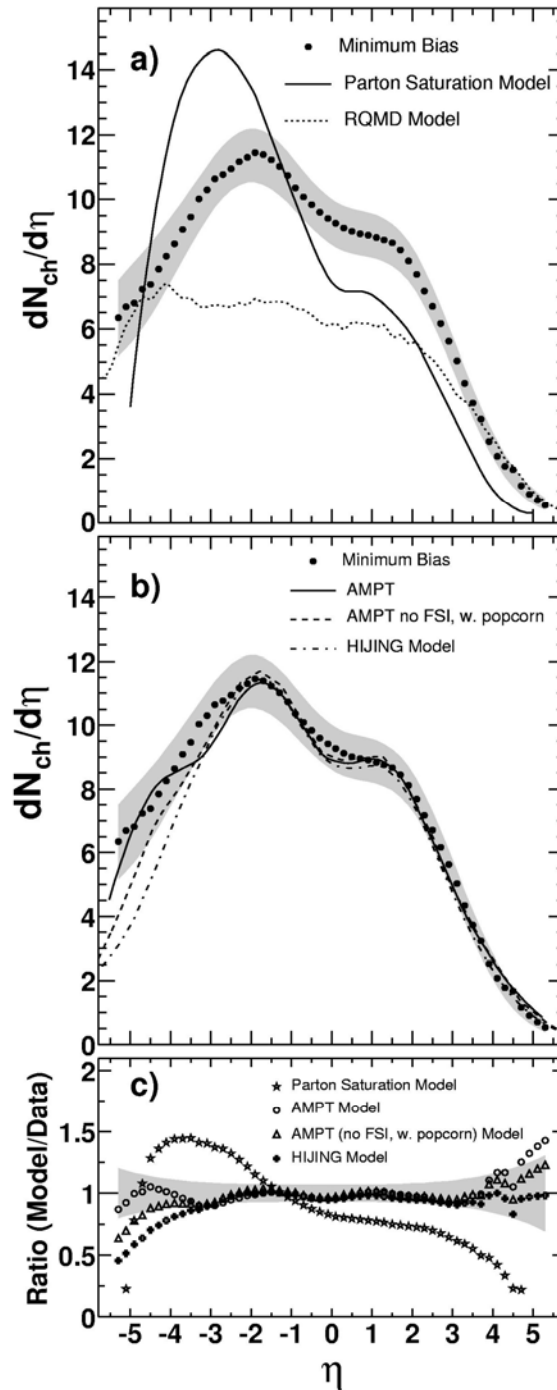


Fig. I-44. Comparison of the measured minimum-bias pseudorapidity distribution for dAu collisions at $\sqrt{s_{NN}}$ to model predictions. a) Comparison to the parton saturation Model¹¹ and RQMD¹⁰. b) Comparison to the predictions of HIJING¹² model and, the published AMPT model with and without final-state interaction (FSI)¹³. c) Quantitative evaluation of the model predictions, expressed as ratio of the model prediction to the data. The gray band corresponds to the systematic errors (90% C.L.) on the data.

However, an alternate explanation of this phenomenon was also put forth. This explanation is based on the Parton Saturation model, which predicts an overall reduction of particle production associated with the expected suppression of the gluon density in the incoming highly relativistic Au-ions. Since the latter effect should also be present if only a single Au nucleus was involved in the collisions, it became very important to study also an asymmetric reaction, such as d + Au, to discriminate between these two models.

In Fig. I-45 we show the invariant cross section for charged particles emitted in 200 GeV d + Au collisions as a function of the transverse momentum, p_T , for four

different centrality bins. In order to determine whether the high- p_T particles are suppressed in d + Au collisions we calculate the so-called nuclear modification factor R_{dAu} , which is the ratio of the d + Au spectrum (scaled to the number of individual nucleon-nucleon collisions, N_{coll}), to the spectrum observed in p + p collisions at the same energy. We show the R_{dAu} ratio for four different centrality bins in Fig. I-46. We observe that R_{dAu} approaches unity at $p_T > 2$ GeV/c even for the most central d + Au collisions. This result indicates that the high- p_T suppression observed in Au + Au collisions (solid curve) is not a consequence of gluon saturation in the approaching Au nuclei, since this suppression was absent in d + Au collisions.

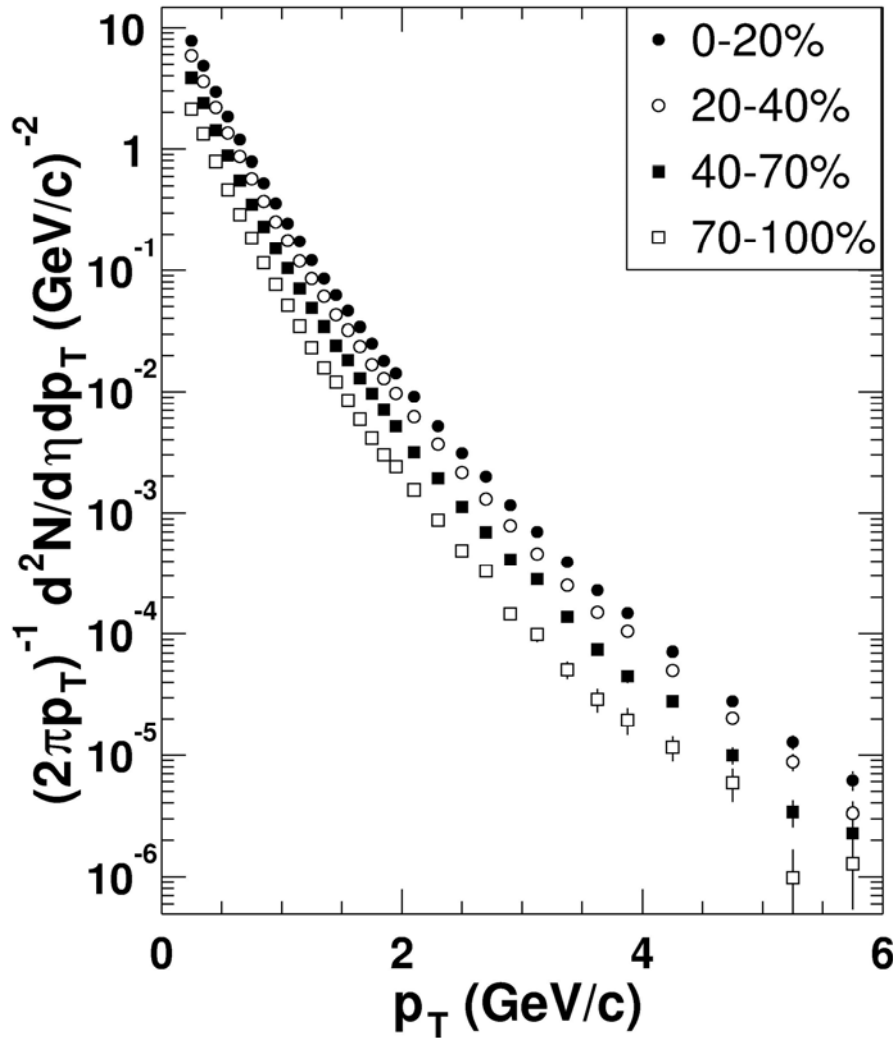


Fig. I-45. Invariant yield of charged hadrons, $(h_+ + h_-)/2$, as a function of p_T for four centrality bins. Only statistical errors are shown (90% C. L.).

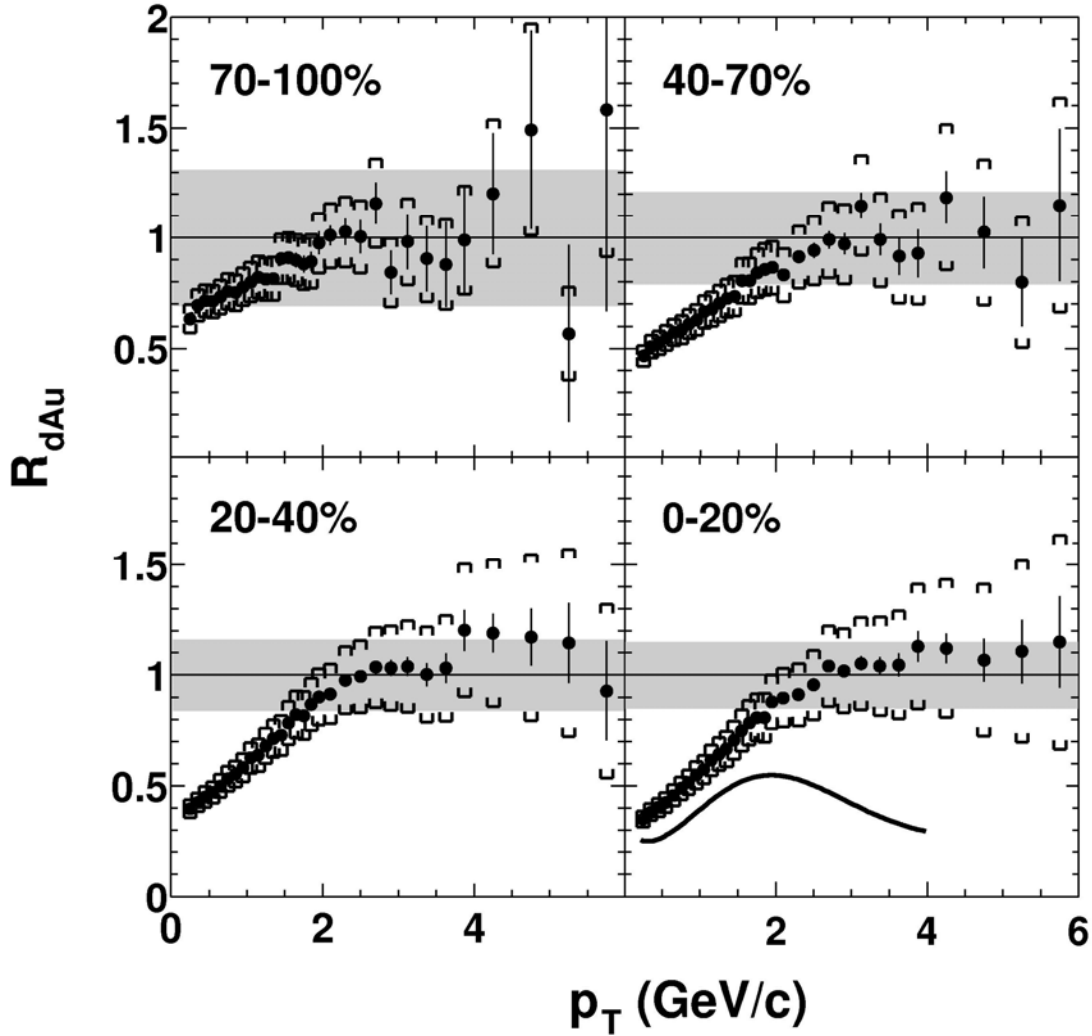


Fig. I-46. Nuclear modification factor R_{dAu} as a function of p_T for four bins of centrality. For the most central bin, the spectral shape for central AuAu data relative to pp is shown for comparison. The shaded area shows the uncertainty in R_{dAu} due to the systematic uncertainty in $\langle N_{coll} \rangle$ and the UA1 scale error (90% C.L.). The brackets show the systematic uncertainty of the dAu spectra measurement (90% C.L.).

f.4. Low Transverse Momentum Spectra in Au + Au Collisions

The PHOBOS spectrometer is designed such that only the 1-mm thick wall of the Be beam pipe separate the interaction region from the first active elements of the Si tracking detectors. This unique feature allows us to study also the very low- p_T part of the particle spectra. The identification of low energy particles is in this case based on the energy loss of particles which traverse the four Si sensors closest to the interaction point and which are stopped in the fifth sensor. Since the six

innermost Si sensors of the spectrometer reside in the field free region, such particles follow straight-line tracks through these sensors. For non-relativistic particles, the specific energy loss, dE/dx , in a single Si layer, i , is $dE/dx \sim 1/\beta^2$, whereas the total particle energy, $E_{tot} = \sum_{k=i}^5 E_k$, i.e. the sum over the energy loss in the remaining Si layers, is given by $E \sim m\beta^2$. A particle identification parameter, M_p , proportional to

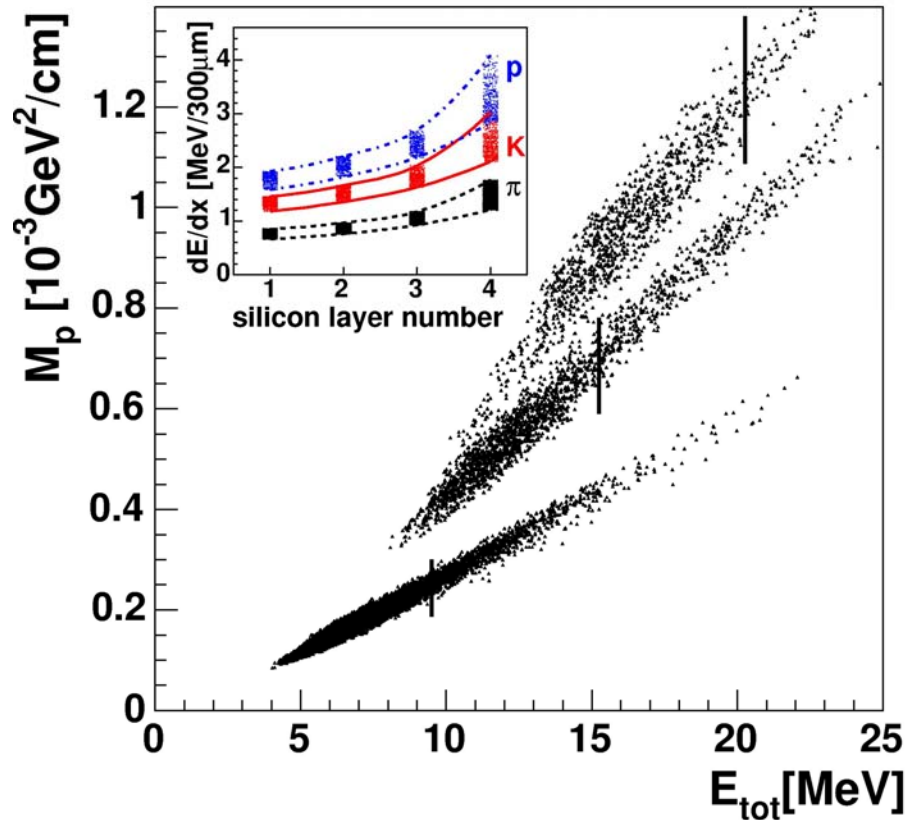


Fig. I-47. (M_p, E_{tot}) scatter plot for the candidate tracks after the $(dE/dx)_i$ cuts in the first four spectrometer layers. Only track candidates with emission angles larger than 60° are shown. The upper limits on E_{tot} are marked by vertical lines. An inset shows 1σ bands on the specific energy loss in the first four Si layers for simulated particles.

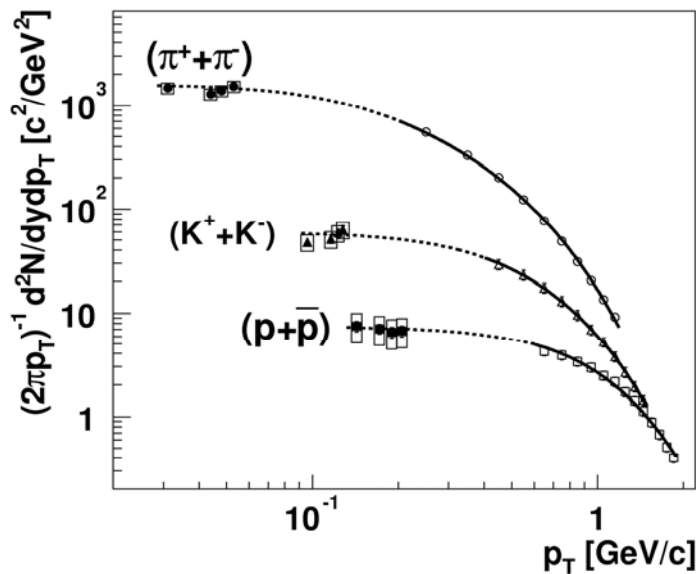


Fig. I-48. Invariant yields as a function of p_T . For low- p_T yields (closed symbols) the boxes show systematic uncertainties. For comparison, the intermediate- p_T measurements from PHENIX¹⁴ are depicted by open symbols. The fits to PHENIX measurements (solid curves) are extrapolated to low p_T (dashed curves). See text for more details.

the particle mass, m , may therefore be obtained as an average of the five quantities $(M_p)_i = (dE/dx)_i \Sigma_{k=1}^5 E_k$, where $i = 1 - 5$. Figure I-47 illustrates the identification of pions, kaons, and protons/anti-protons based on M_p plotted as a function of the total particle energy, E_{tot} . It is evident that this analysis method is able to separate the three particle species.

Having obtained particle identification, the data can be sorted into separate p_T bins based on E_{tot} and the emission angle after corrections for the particle detection efficiency and solid angle coverage, which was obtained by detailed Monte Carlo simulation studies. The results are shown as solid points in Fig. I-48 and compared to measurements of identified particle

spectra by PHENIX covering a higher p_T range. The dashed curves represent an extrapolation to lower p_T of analytical fits (solid curves) of the form $A[\exp(m_T/T_{fit}) + \varepsilon - 1]$ to the PHENIX data. Here m_T is the transverse mass, A and T_{fit} are fit parameters and $\varepsilon = -1$ for mesons and $\varepsilon = +1$ for baryons.

The measurement of the low- p_T particles does not indicate any enhancement of this part of the spectrum as was suggested theoretically. On the contrary, the observed spectral forms are consistent with a transverse expansion of the system leading to a suppression of the low- p_T part of the spectra.

*Brookhaven National Laboratory, Institute of Nuclear Physics, Krakow, Poland, Massachusetts Institute of Technology, National Central University, Taoyuan, Taiwan, University of Rochester, University of Illinois at Chicago, and University of Maryland.

¹B. B. Back *et al.*, (PHOBOS) Phys. Rev. Lett. **91**, 052303 (2003).

²G. J. Alner *et al.*, Z. Phys. C **33**, 1 (1986).

³A. S. Goldhaber, Phys. Lett. **B53**, 306 (1974).

⁴W. D. Myers and W. J. Swiatecki, Ark. Fys. **36**, 343 (1967).

⁵J. Barrette *et al.*, Phys. Rev. C **45**, 819 (1992).

⁶W. Thome *et al.*, (ISR), Nucl. Phys. **B129**, 365 (1977).

⁷F. Abe *et al.*, Phys. Rev. D **41**, 2330 (1990).

⁸B. B. Back *et al.*, (PHOBOS), Phys. Rev. Lett. **85**, 3100 (2000).

⁹S. V. Afanasiev *et al.*, Phys. Rev. C **66**, 054902 (2002); T. Anticic *et al.*, Phys. Rev. C **69**, 024902 (2004).

¹⁰H. Sorge, Phys. Rev. C **52**, 3291 (1995).

¹¹D. Kharzeev *et al.*, arXiv:hep-ph/0212316.

¹²M. Gyulassy and X. N. Wang, Comp. Phys. Comm. **83**, 307 (1994).

¹³Zi-wei Lin and Che-ming Ko, arXiv:nucl-th/0301025.

¹⁴S. S. Adler *et al.* (2003) submitted to Phys. Rev. C, arXiv:nucl-ex/0307022.